Volume 1 | Number 1 | Jan 2013 | Pages 1–100

Journal of
Materials Chemistry A

Materials for energy and sustainability
www.rsc.org/materialsA

Li⁺

ROYAL SOCIETY
OF CHEMISTRY

ROYAL SOCIETY
OF CHEMISTRY

www.rsc.org/materialsA

Journal Name

ARTICLE

Synergistic Effect of Three-dimensional Orchid-like TiO$_2$ Nanowire Networks and Plasmonic Nanoparticles for Highly Efficient Mesoscopic Perovskite Solar Cells

Haejun Yu, Jongmin Roh, Juyoung Yun and Jyongsik Jang[*]

TiO$_2$ nanoparticle (TiO$_2$ NP)-based mesoscopic electron transport structures have been frequently used in organic–inorganic hybrid perovskite solar cells (PSCs) for rapid electron transport. However, TiO$_2$ NPs that are densely agglomerated in the scaffold layer may inhibit the penetration of a perovskite solution thereby deteriorating the device performance. Here, we use three-dimensional orchid-like TiO$_2$ nanowires (OC–TiO$_2$ NWs) as scaffold materials to overcome the deficiencies of TiO$_2$ NP-based structures. The perovskite precursor deeply infiltrated into the spacious pores within the OC–TiO$_2$ NW network and crystallized in the scaffold layer, which increased recombination resistance and charge extraction efficiency. Additionally, Ag NPs were introduced in the form of an silica-coated Ag@OC–TiO$_2$ NW (SiO$_2$@Ag@OC–TiO$_2$ NW) composite to achieve still better performance through localized surface plasmon resonance (LSPR) and exciton dissociation inducement of the Ag NPs. Consequently, a PSC based on this collaborative scaffold consisting of Ag NPs and OC–TiO$_2$ NWs exhibited a high power conversion efficiency (PCE) of 15.09 %, which is an improvement of 24 % over a PSC based on a TiO$_2$ NP scaffold layer, where the average PCE was 12.17 %.

Introduction

A new trend in the photovoltaics field, of using organic–inorganic hybrid perovskites as light absorbers in solar cells, began in 2012 with the report by Park et al. of a 9 % power conversion efficiency (PCE).[1] The perovskite absorber has many advantages that include outstanding optical properties,[2] ambipolar charge transport, a high absorption coefficient, long charge diffusion length, excellent crystallinity[3] and high tolerance to chemical defects.[4] Numerous studies have explored ways to improve the performance of perovskite solar cells (PSCs), and have achieved significant advancement through control of the structural type, deposition skills and chemical tuning of the perovskite absorber. Consequently, a PCE of 20 % was recently achieved with a mesoscopic structure.[5]

Several kinds of architectures have been used in PSCs, including inverted,[6] planar,[6] mesoscopic,[7] and meso-superstructured.[8] The mesoscopic sensitized structures using semiconducting metal oxides such as TiO$_2$,[1] ZnO,[9] SnO$_2$[10] and WO$_3$ NPs[11] facilitate transport of the extracted electron to a fluorine-doped tin oxide (FTO) substrate. Notably, one- or

multi-dimensional TiO$_2$ materials have been widely used in dye-sensitized solar cells (DSSCs) as an electron transport layer (ETL) because of their better electrical and constructional properties compared with TiO$_2$ NPs.[12-14] Recently, rutile TiO$_2$ nanofibers and nanorods were used as the scaffold structure in a PSC as well as a DSSC, achieving PCEs of 9.8 %[15] and 9.4 %[16], respectively. Furthermore, unique TiO$_2$ nanostructured PSCs such as dendritic,[17] cone-like[18] and three-dimensional architectural TiO$_2$ have been used as ETLs,[19] which has gradually enabled photovoltaic performance to improve toward the PCE of 13.25 % that is a similar level with TiO$_2$ NP-based PCE. However, their performances are still lower than those of NP-based devices; research and development has been tardy in the PSC field. Hence, one- or multi-dimensional nanomaterials-based ETL needs to be explored to improve the performance of PSCs.

Many types of solar cells have introduced plasmonic materials to upgrade photovoltaic performance by leveraging the optical, electronic and magnetic properties of noble metals.[20] Notably, Ag and Au NPs have often been chosen for their plasmonic effects in DSSCs[21-23] and PSCs. Snaith et al. reported a PCE of 11.4 % after adding small amounts of Au@SiO$_2$ core-shell NPs into an Al$_2$O$_3$-based scaffold layer to enhance the current density. Sun et al. also announced a PCE of 16.2 % with insertion of Au NPs into the ETL, revealing that hot electrons improve the internal operation of PSCs.[24] These improvements with Au NPs were mainly attributed to the improved exciton dissociation and thermal effect of the Au NPs. Additionally, the LSPR effect of Au NPs can contribute to performance enhancement. The noble metals can amplify the

School of Chemical and Biological Engineering,
Seoul National University, 599 Gwanangno, Gwanakgu, Seoul 151-742, Korea
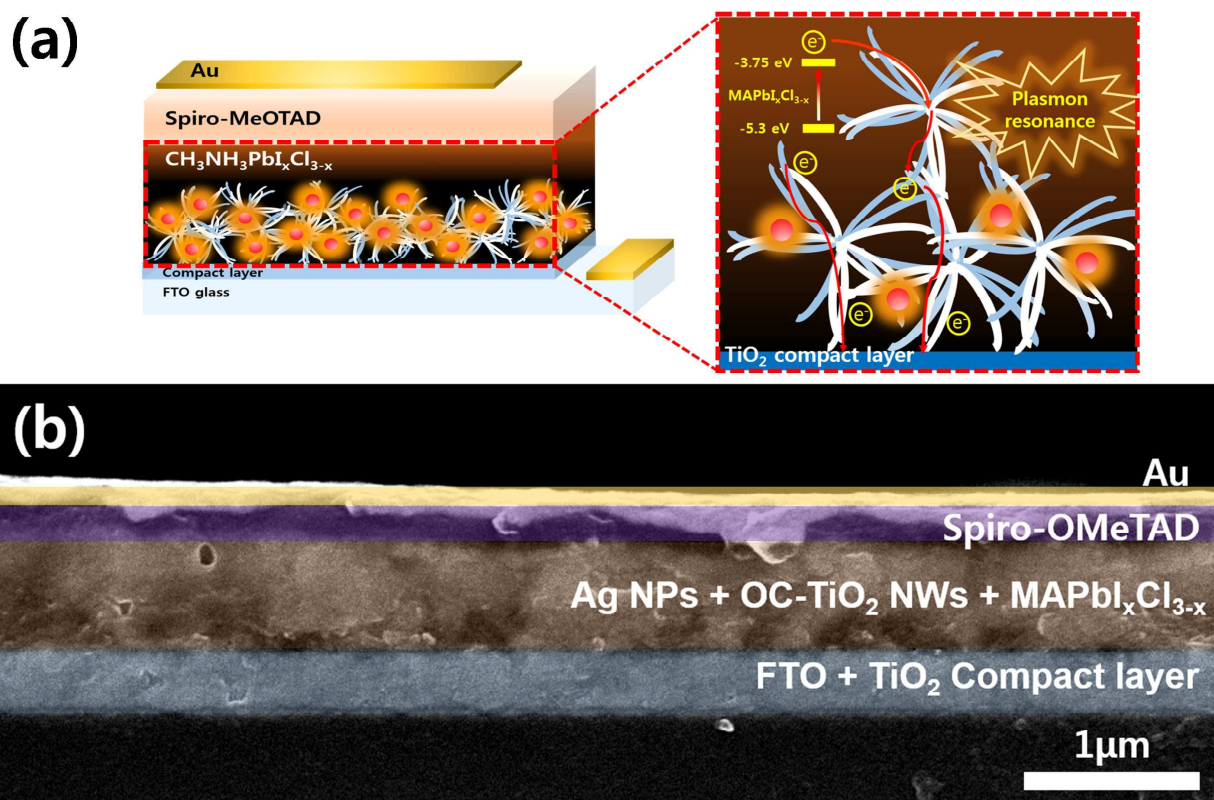*E-mail: jsjang@plaza.snu.ac.kr ; Fax: +82 2 880 1604; Tel: +82 2 880 7069*

Fig 1. (a) Schematic diagrams symbolizing the various layers of a perovskite solar cell (PSC) having a scaffold layer consisting of SiO_2@Ag@OC–TiO_2 NWs and OC–TiO_2 NWs and illustrating the direct pathway of electrons in the OC–TiO_2 NWs and the plasmonic effect by the Ag NPs decorated on the OC–TiO_2 NWs. (b) Scanning electron microscopy (SEM) image displaying a cross-sectional view of a PSC based on the same scaffold structure.

electromagnetic field through oscillation between the electromagnetic field and conducting electrons.[23] Furthermore, the light scattering effect of Au NPs by resonant scattering of incident light may increase the optical path length of the solar cell, thereby increasing light absorption. [25] However, using Ag NPs in PSCs has hardly been reported, although Ag NPs have similar plasmonic effects.

Herein, we design a synergistic ETL combining multi-dimensional TiO_2 nanomaterials with Ag NPs for improved PSC performance. Highly crystalline anatase orchid-like TiO_2 nanowires (OC–TiO_2 NWs) replaced TiO_2 NPs as the electron transport materials in the scaffold layer. This substitution caused very dense crystallization of perovskite by full pore-filling and provided fast charge transport via long wires of OC-TiO_2 and continuous perovskite phase. Additionally, Ag NPs were introduced as co-agents into the OC–TiO_2 NW network in the form of silica-coated Ag@OC–TiO_2 NWs (SiO_2@Ag@OC–TiO_2 NW), thereby enhancing light harvesting by plasmonic effects. This synergistic combination led to a steep improvement of the average performance in comparison with control device, and a PCE of 15.09 % was achieved by the addition of optimal amounts of SiO_2@Ag@OC–TiO_2 NWs into an OC–TiO_2 NW-based ETL with MAPbI$_x$Cl$_{3-x}$ as a perovskite sensitizer.

Result and discussion

The PSC based on our scaffold engineering is depicted schematically in Fig. 1a. The compact layer was spin-coated on fluorine-doped tin oxide (FTO) at a thickness of 50 nm to prevent direct contact between the FTO and the hole-conductor. The OC–TiO_2 NW network was constructed hierarchically on a compact layer to a height of *ca.* 400 nm. The structural details of an OC–TiO_2 NW-based ETL are shown schematically in the red-dashed box of Fig. 1a; the random stacks of OC–TiO_2 NWs generated wide pores in the film, thereby enabling excellent penetration of perovskite into the ETL. Rapid charge transport by a straight conduction pathway of the OC–TiO_2 NWs is also indicated in that box; the number of interparticle boundaries was considerably diminished by substituting TiO_2 NPs with OC–TiO_2 NWs. Concurrently with using OC–TiO_2 NWs as the ETL, small amounts of SiO_2@Ag@OC–TiO_2 NWs were added into the ETL to enhance light absorption by the plasmonic effects. After sintering at 500 °C to remove contaminants on the TiO_2 surface without morphological damage to OC–TiO_2 NWs (Fig. S1), the film was immersed in the 20 mM of $TiCl_4$ aqueous solution to improve inter-connectivity among the OC-TiO_2 NWs. Then, MAPbI$_x$Cl$_{3-x}$ and Spiro-MeOTAD films were spin-coated as a light absorber
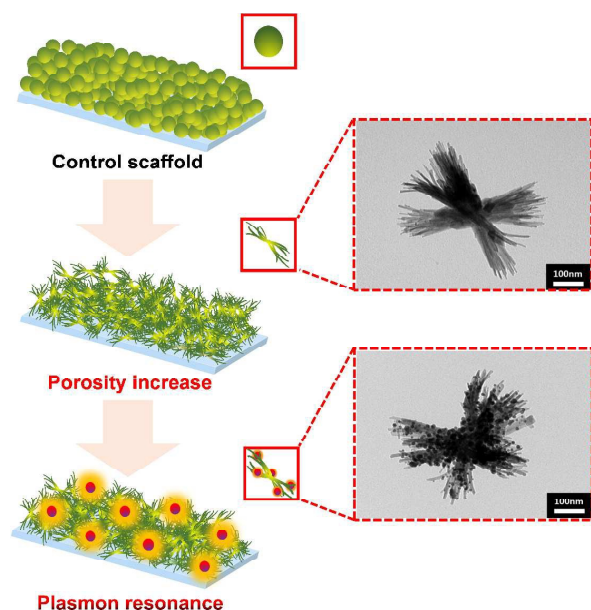
ARTICLE

Figure 2. Illustration of stepwise changes from a TiO₂ NP-based scaffold layer to an OC–TiO₂ NW-based one and finally to an Ag/OC–TiO₂ NW-based scaffold layer. The inset images are transmission electron microscope (TEM) images of OC–TiO₂ NWs and SiO₂@Ag@OC–TiO₂ NWs.

and hole transport material (HTM), respectively. Finally, Au was thermally deposited to complete the assembly.

Fig. 1b exhibits a cross-sectional field-emission scanning electron microscopy (FE-SEM) image of the completed device. The respective layers are distinguished by different colors. The uniformly deposited OC–TiO₂ NWs and SiO₂@Ag@OC–TiO₂ NWs were fully surrounded by the tightly packed perovskite film. Also, X-ray diffraction (XRD) measurements and a top-view FE-SEM image verified that the perovskite film was deposited with full coverage and with high crystallinity. (Fig. S2 and S3)

Fig. 2 delicately represents the transition of the scaffold structure from a TiO₂ NP-based scaffold to an OC–TiO₂ NW-based one and finally to the case where SiO₂@Ag@OC–TiO₂ NWs were added to the OC–TiO₂ NW-based scaffold. We abbreviate the final case as "Ag/OC–TiO₂ NW" for a concise expression of the structure. At first, the cramped scaffold layer made with TiO₂ NPs contained fairly narrow pores. The perovskite precursor was unable to completely penetrate into these tight voids [26] (Fig. S4) and the empty spaces formed by imperfect penetration of the perovskite precursor resulted in high voltage loss by recombination at the interface between the TiO₂ NPs and the hole-conductor.[7] There were also numerous disconnected boundaries when TiO₂ NPs were used for the scaffold layer, which led to unfavorable charge transport, even if a calcination process was followed to ensure tight coupling among adjacent TiO₂ NPs. In contrast to TiO₂ NPs, larger and longer TiO₂ nanomaterials generated relatively broad pore volumes and small numbers of interconnected boundaries due to the expanded scale of the building

materials; this is suitable for electron transport for smooth movement of electric charges.[27] Thus, a multi-dimensional structure constructed with larger TiO₂ nanomaterials was anticipated to reduce the recombination and charge transport resistance with improving the performance of PSC. In this approach, TiO₂ NPs were replaced with three-dimensional OC–TiO₂ NWs to improve the pore-filling and charge transport.

The OC–TiO₂ NWs were synthesized by solvothermal reaction using dimethylformamide (DMF) and acetic acid (HAc) as organic solvents with a lithium salt as additive. A ratio of 5/5 v/v solutions of DMF/HAc was more favorable because it provided a high proportion of the anatase phase, which assured a rapid electron transport rate and a high electron diffusion coefficient.[28] (Fig. S1a) Specific surface area and pore size distribution were obtained by Brunauer–Emmett–Teller (BET) measurement and Barrett–Joyner–Halenda (BJH) desorption pore distribution plots, respectively. (Fig. S5a-c, Table S1). In addition, the roughness factor (R_f) of each film was evaluated from dye adsorption/desorption method by combining with UV-Vis absorbance measurement and Beer-lambert law. (Fig S5d, Table S2) The specific surface area and roughness factor of an OC-TiO₂ NW-based film (61.95 m²/g, 189.8) were slightly smaller than those of a TiO₂ NP-based film

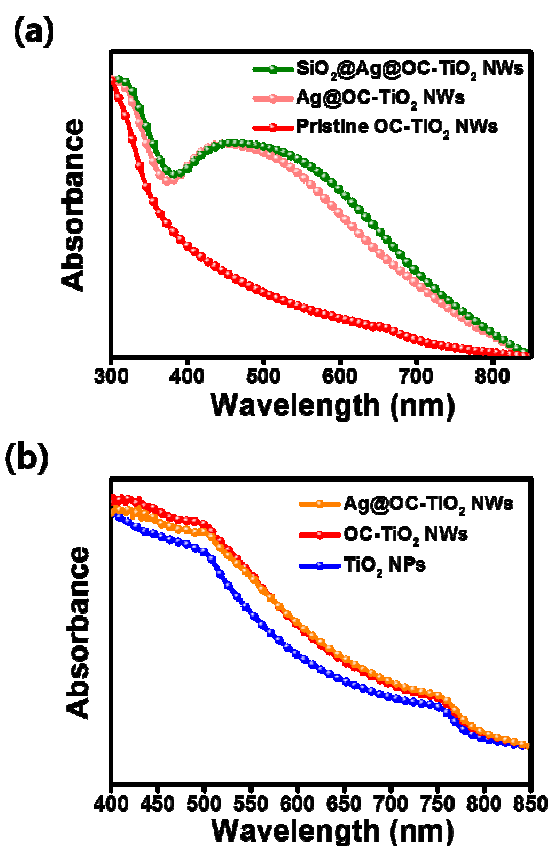**Fig. 3.** (a) UV–Vis absorbance spectra of OC–TiO₂ NWs, Ag@OC–TiO₂ NWs and SiO₂@Ag@OC–TiO₂ NWs. (b) UV–Vis absorbance of MAPbIₓCl₃₋ₓ films deposited on scaffold layers consisting of TiO₂ NPs, OC–TiO₂ NWs or Ag/OC–TiO₂ NWs.

(78.44 m^2/g, 111.2) due to spacious void of OC-TiO$_2$ NW-based film and a relatively big size of OC-TiO$_2$ NW. Even though the factors are quite important for electron extraction or contact between TiO$_2$ and perovskite,[29] the other factors except surface area could offset this disadvantage of OC-TiO$_2$ NW-based film. OC-TiO$_2$ NW-based film having lots of wide pores (> 40 nm) improves the pore-filling and loading amount of perovskite compared with diminutive TiO$_2$ NPs, which greatly increases recombination resistance and incident light absorption. Furthermore, contrary to working principle of dye-sensitized solar cell, the electrons excited in perovskite can sufficiently migrate to charge selective layers in perovskite phase due to an ambipolar transport property[3] and long electron diffusion length of MAPbI$_x$Cl$_{3-x}$.[30]

To further enhance the device performance, the plasmonic NPs were introduced in the form of SiO$_2$@Ag@OC–TiO$_2$ NW composites, which improved photovoltaic performance in several aspects. First, the LSPR effect plays a pivotal role in improvement of light concentration by storing the incident energy in a localized surface plasmon mode; the electromagnetic field near the Ag NPs is significantly enhanced at a wavelength resonant with electron oscillation.[31-34] By the LSPR effect, the absorption rates of perovskite near metal NPs are augmented through the stored energy conversion from metal to perovskite, and incident light absorption and charge generation are improved.[23] Second, the introduction of Ag NPs assists in reducing the exciton binding energy of perovskite owing to the subtleties of exciton-plasmon coupling. A free charge carrier can be generated easily through facile ionization of excitons in the presence of Ag NPs.[8] These two factors can be dominantly affective to performance improvement. Except for the main factors, the light absorption-induced plasmonic heating effect, attributed to photocurrent improvement, can lead to advanced local mobility of the charge carrier.[35] This effect promotes an electrochemical behavior of free charges in the photovoltaic device, increasing the photocurrent density without noticeable spectral dependence.

Fig. S6a shows a transmission electron microscope (TEM) image of SiO$_2$@Ag@OC–TiO$_2$ NWs. The Ag NPs were closely spaced on the OC–TiO$_2$ NWs and had a narrow size distribution. As shown in Fig. S6b, the fabricated Ag NPs had

an average diameter of *ca*. 10 nm. The form of the OC–TiO$_2$ NWs was unchanged after binding of the Ag NPs. In Fig. S6c, XRD was measured for a more accurate confirmation of the synthesized Ag@OC–TiO$_2$ NWs. Except for diffraction peaks of anatase TiO$_2$, the diffraction peaks were observed at *ca*. 38°, 44°, 64° and 77° for the Ag NPs, which exactly matched the crystal planes of Ag NPs.[36]

UV–visible (UV–Vis) absorption spectroscopy was used to investigate the plasmonic characteristics in detail. The absorption edge of pristine OC–TiO$_2$ NWs was *ca*. 400 nm and was only weakly absorbed over most of the visible light range. The Ag@OC–TiO$_2$ NWs had a resonance peak at 450 nm in ethanol. (Fig. 3a) To prevent the degradation of Ag NPs during calcination, the protective SiO$_2$ shell was coated on the Ag NPs, causing a slight red-shift of extinction spectrum; this may be related to a change in the local refractive index. The thickness of protecting SiO$_2$ shell was *ca*. 7 – 9 nm (Fig. S6a) which contributed to high intensity of LSPR band and excellent performance of PSC.[23] This SiO$_2$ shell functioned as a shield to prevent direct contact between Ag NPs and the hole-transfer materials and to reduce the risk of performance deterioration.[37]

The UV–Vis absorption spectrum of the perovskite absorber was used to monitor its effective penetration into scaffold layer. Fig. 3b indicates the light absorption spectra of the perovskite deposited on TiO$_2$ NP-, OC–TiO$_2$ NW- and Ag/OC TiO$_2$ NW-based scaffolds having the same thickness. The perovskite film on the TiO$_2$ NP-based scaffold absorbed much less amounts of light than the other cases because the perovskite precursor could not permeate into every nook and cranny of that scaffold. (Fig. S7) In contrast, the wide pores within the OC–TiO$_2$ NW scaffold assisted substantial loading[38] and penetration of the perovskite precursor to the bottom of the ETL and thereby augmented the harvesting of incident light and soaking of the charge carrier inside the mesoscopic perovskite layer.[39] However, there was a negligible difference in light absorption between the OC–TiO$_2$ NWs and the Ag/OC–TiO$_2$ NWs cases. This result was because the optimized quantities of Ag NPs were very low to increase the light absorbance of the film.
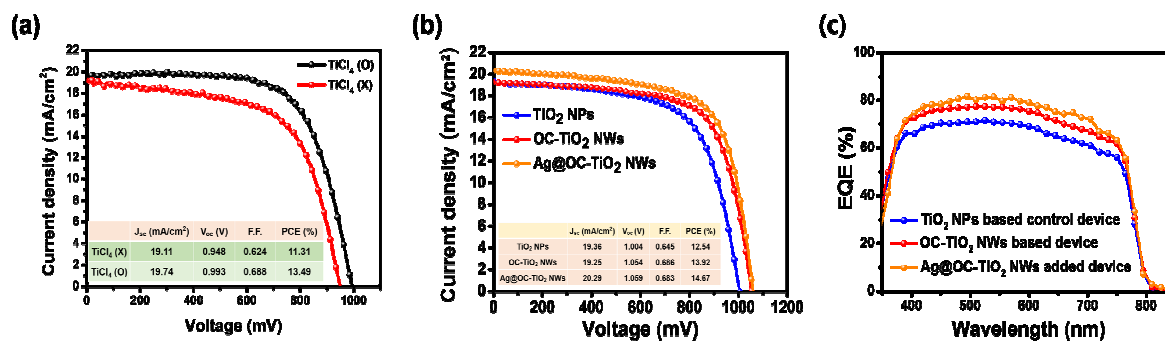

Fig. 4. (a) J–V curves of PSCs based on OC–TiO$_2$ NWs scaffold layer. The black line is post-treated with TiCl$_4$ of 20 mM and red line is not post-treated with TiCl$_4$. (b) J–V curves and (c) eternal quantum efficiency (EQE) spectra of PSCs based on scaffold layers consisting of TiO$_2$ NPs, OC–TiO$_2$ NWs and Ag/OC–TiO$_2$ NWs.
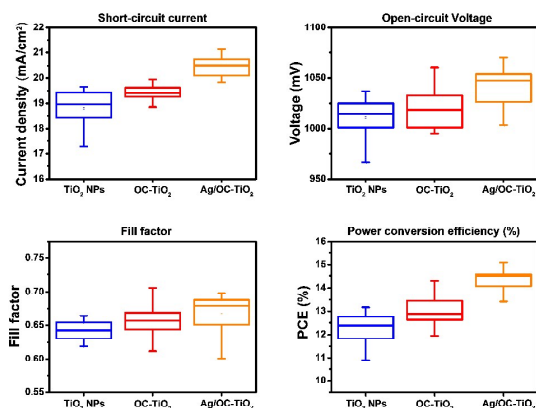
ARTICLE

Fig. 5. Comparison of the photovoltaic parameters of PSC devices measured for 20 devices for each ETL.

We examined time-resolved photoluminescence (PL) spectra of the $MAPbI_xCl_{3-x}$ film on each of the three TiO_2 scaffold layers (Fig. S8). The PL emission quenching was slightly reduced with the replacement of scaffold layer from TiO_2 NPs to OC–TiO_2 NWs. It signifies that the charges dissociated from the perovskite excitons easily migrated into the TiO_2 NP-based structure, because of the high surface area of TiO_2 NPs. Although the electron extraction itself was less efficient in OC-TiO_2 NW-based scaffold, this disadvantage could be offset by other merits of the OC-TiO_2 NW-based scaffold sufficiently. High loading amount of perovskite, a formation of continuous perovskite film by great pore filling and a direct charge pathway through long wires are outstanding merits of OC-TiO_2 NW-based film. Moreover, the electron extraction efficiency was more facilitated with the incorporation of Ag NPs due to decrease in exciton binding energy of perovskite. This effective ionization of excitons could enhance charge separation and photocurrent density.[8]

To scrutinize the performance of the complete PSCs device based on different ETLs, the typical J-V curves were characterized under illumination conditions of AM 1.5 G 100 mW/cm². Fig. 4a demonstrates that redesigning the scaffold layer using OC–TiO_2 NWs and Ag/OC–TiO_2 NWs improves most of the photovoltaic parameters. The PSCs with the TiO_2 NP-based scaffold layer exhibited an open-circuit voltage (V_{oc}) of 1.004 V, a short-circuit current density (J_{sc}) of 19.36 mA/cm², a fill factor (FF) of 0.645 and a PCE of 12.54 %. Simultaneously with substituting the TiO_2 NPs with pristine OC–TiO_2 NWs, we checked out the effect of post-treatment to make up for the weak points of OC-TiO_2 NW-based film. (Fig. 4a, Table S3) To overcome the relatively poor inter-connection of OC-TiO_2 NWs and the frequent back recombination,[40] $TiCl_4$ post-treatment was carried out,[27] leading to more efficient electron transfer through new bridges between the inter-particle boundaries. After the replacement, the V_{oc} and FF were noticeably improved to 1.054 V and 0.686, respectively. Then, a very low weight of Ag NPs was added to the OC–TiO_2 NW-based paste in the form of SiO_2@Ag@OC–TiO_2 NW and the optimal weight was determined by varying the amount of the Ag NPs. (Fig. S9)

The performance was gradually improved by adding Ag NPs up to 0.75 wt%, but then sharply declined above this addition level. This behavior was attributed to an increased light absorption caused by large amounts of Ag NPs, which can induce the trapping of photogenerated electrons and convert incident light into heat energy.[41] By adding the optimized amount of Ag NPs (0.75 wt%) into the OC–TiO_2 NW-based ETL, the J_{sc} increased from 19.36 to 20.29 mA/cm² because of the LSPR and various plasmonic effects; the PCE reached 14.67 %, the V_{oc} was 1.059 V and the FF was 0.683. Such modification of the ETL increased the PCE by *ca.* 17 %. The slightly increased V_{oc} was attributed to the insulating SiO_2 coating: charge recombination at the photoanode interface could have been retarded by the SiO_2 coating, and the separated electron and hole could have moved along a direct pathway inside the perovskite. Therefore, an unnecessary charge migration step at the TiO_2/perovskite interface was removed at the SiO_2 regions, at which voltage loss was partially mitigated.

External quantum efficiency (EQE) was measured for the three types of devices to certify their photovoltaic performances (Fig. 4c). The EQE results were in good agreement with the electrical characteristics of each type of device. The OC–TiO_2 NW-based device displayed enhanced quantum efficiency over the whole range of visible wavelengths. We speculated that the effective infiltration and large loading amount of perovskite induced the results. The addition of SiO_2@Ag@OC–TiO_2 NWs intensified the EQE spectrum over the whole visible region (400–750 nm) because of the increase of photocurrent caused by the plasmonic-enhanced light harvesting by the Ag NPs.

To check out the reliabilities of our scaffold-engineered PSCs, the average photovoltaic parameters were obtained from 20 other devices. (Fig. 5 and Table S4) The average trend of the parameters was similar to that of the sample devices compared in Fig. 4a. The average PCE of the TiO_2 NP-based devices was 12.17 %, with a J_{sc} of 18.82 mA/cm², a V_{oc} of 1.011 V and an FF of 0.639. However, when the TiO_2 NPs were replaced with OC–TiO_2 NWs, the average PCE was 12.97 %, with a J_{sc} of 19.44 mA/cm², a V_{oc} of 1.020 V and an FF of 0.654.
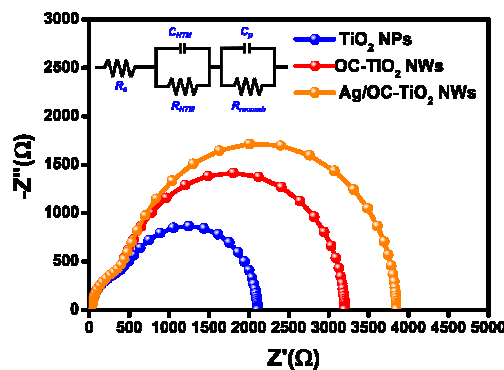

Fig. 6. Nyquist plots of the complete devices based on ETLs consisting of TiO_2 NPs, OC–TiO_2 NWs and Ag/OC–TiO_2 NWs. The measurements were made in the dark at a 0.7 V bias voltage.
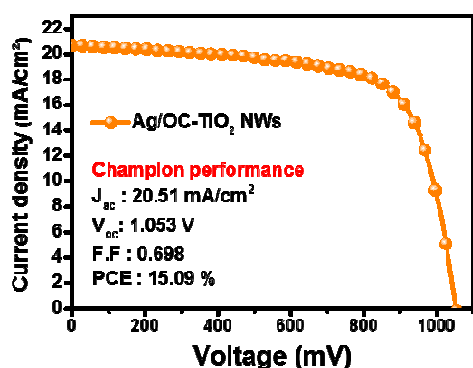
Fig. 7. The champion performance of PSCs based on an ETL consisting of Ag/OC–TiO₂ NWs.

Through the insertion of $SiO_2@Ag@OC–TiO_2$ NWs, the devices exhibited an average PCE of 14.18 %, a J_{sc} of 20.46 mA/cm^2, a V_{oc} of 1.040 V and an FF of 0.666. These enhancements resulted from the reduction of recombination by excellent pore filling, and from small voltage loss by direct electron transport to charge selective contact through bulk perovskite phase crystallized in the wide pore.[42] Furthermore, it is likely that the silica coated-Ag NPs increased the photocurrent density by a plasmonic-enhanced light absorption and a local heating effect. Independent of the effects induced by light absorption, the reduced exciton binding energy of the perovskite with the incorporation of the Ag NPs improved the electron generation and injection efficiency, and increased the short-circuit current.[8]

Electrochemical impedance spectroscopy (EIS) from 1 Hz to 1 MHz was used to characterize the charge transport process delicately. Fig. 6 denotes Nyquist plots of the impedance spectra for devices prepared with different scaffold layers, and an equivalent circuit was employed to fit the plots. In the equivalent circuit model, the interface resistance of FTO is expressed as R_s and the recombination resistance and chemical capacitance are related to R_{recomb} and C_μ, respectively. The R_{HTM} and C_{HTM} are related to the interface of counter electrode and its capacitance.[43] The small arc in the high frequency region is associated with counter electrode resistance. There was no significant difference on the size of arc and value of R_{HTM} because the identical fabrication process was applied to HTM coating and Au deposition.[44] The main arc in low frequency region was caused by resistance of ETL/perovskite/HTM interface. With the replacement of scaffold material from TiO_2 NP to OC-TiO₂ NW or Ag/OC-TiO₂ NW, recombination resistance was increased. The R_{recomb} value of TiO_2 NP-based PSC was 1668 Ω, and the value was increased to 2795 Ω and 3404 Ω for OC-TiO₂ NW and Ag/OC-TiO₂ NW-based PSC, respectively. The reduced recombination between the TiO_2 and the HTM was ascribed to excellent pore-filling of the perovskite. The resistance of recombination was increased by the addition of $SiO_2@Ag@OC–TiO_2$ NWs into the ETL, which may be related to rapid electron extraction and transport

caused by decrease of exciton binding energy of the perovskite. In addition, Schottky barrier at Ag/OC-TiO₂ NW interface can considerably suppress charge recombination reaction between TiO_2 and HTM.[45]

The highest-performing device made with our scaffold engineering approach exhibited a PCE of 15.09 % by reverse scan under AM 1.5 G illumination, and a J_{sc}, V_{oc} and FF of 20.51 mA/cm^2, 1.053 V and 0.698, respectively (Fig. 7). The variation in the PCE was within 6.5 % and was affected by the light intensity, spectrum mismatch, a testing mask aperture effect and the laboratory environment, all of which affected the sensitivity of the perovskite.[46] Compared with the device with a scaffold layer based on TiO_2 NPs, decorating the Ag/OC–TiO₂ NWs in the ETL enhanced the PCE by *ca.* 24 %. This notable result may stem from a synergistic effect between the noble metal and the one-dimensional nanomaterials.

Conclusions

Summarizing, we successfully designed a unique ETL using Ag NPs and TiO_2 NWs with orchid-like morphology. The penetration of the perovskite solution was enhanced due to the large pore size among the OC–TiO₂ NWs, minimizing detrimental voids in the ETL and providing a higher voltage and FF. A comparable current density could be obtained by a straight charge transport pathway because of the one-dimensional OC–TiO₂ NWs network. The current density was also increased by plasmonic-enhanced light absorption and the increased recombination resistance. Consequently, our scaffold engineering approach provided a highest PCE of 15.09 % and an average PCE of 14.18 %. Careful design for the most efficient ETL is expected to lead to the fabrication of advanced PSCs with greatly enhanced performance.

Experimental Section

Preparation of OC–TiO₂ NWs by hydrothermal reaction

The OC–TiO₂ NWs were synthesized by a slightly modified hydrothermal method according to the method described previously.[47] Lithium chloride (LiCl; 0.2 g, Sigma–Aldrich) was mixed with 10 mL of DMF (99.5 %, Junsei Chemical) and HAc (99.5 %, Oriental Chemical Industries). A mixed organic solvent (DMF/HAc, 5/5 v/v) provided the best performance of the OC–TiO₂ NWs in the device. After dissolving lithium chloride in the mixed solvent, titanium (IV) butoxide (TB; 2 mL, reagent grade, 97 %, Sigma–Aldrich) was added to the organic solution. Then, the precursor solution was transferred into a Teflon-lined stainless steel autoclave and heated at 200 °C in an oven for 20 h. The final products, OC–TiO₂ NWs, were washed with acetone and ethanol several times and dried in an oven at 70 °C for 10 h.

Preparation of Ag@OC–TiO₂ NWs

The OC–TiO₂ NWs (100 mg) were dispersed in absolute ethanol (10 mL, Fisher). Then, 3-mercaptopropyltrimethoxysilane

(MPTS; 20 μL, Sigma–Aldrich) and ammonium hydroxide (50 μL, Sigma–Aldrich) were added and the solution was stirred at room temperature for 12 h. The MPTS-treated OC–TiO$_2$ NWs were centrifuged at 10,000 rpm and washed with ethanol several times. The OC–TiO$_2$ NWs (100 mg) treated by MPTS were dispersed in ethylene glycol (100 mL, Sigma–Aldrich) followed by stirring for 1 h at room temperature. Silver nitrate (51 mg, Sigma–Aldrich) was added to the solution to attach the Ag NPs to the OC–TiO$_2$ NWs. Finally, octylamine (0.05 mL, Sigma–Aldrich) was quickly added to the solution, which was stirred for 1 h at room temperature. The OC–TiO$_2$ NWs decorated with the Ag NPs were obtained by centrifugation and washed free of impurities with ethanol.

Preparation of SiO$_2$@Ag@OC–TiO$_2$ NWs

The fabrication method of the thin silica shell was reported previously.[48] The prepared Ag@OC–TiO$_2$ NWs were dissolved in distilled water (30 mL) and polyvinylpyrrolidone (PVP; 0.1 g, MW = 40,000, Sigma–Aldrich) was added, followed by stirring for 1 h. The suspension was adsorbed by the PVP, which was collected by centrifugation and washing. The obtained products were redispersed in absolute ethanol (13.17 mL) and mixed with ammonium hydroxide (0.65 mL, Sigma–Aldrich) and distilled water (0.23 mL). Finally, tetraethyl orthosilicate (TEOS; 60 μL, Sigma–Aldrich) was quickly added and the solution was stirred for 4 h at 35 °C. The final product was obtained after centrifugation and washing.

Preparation of the TiO$_2$ NWs paste

The as-prepared OC–TiO$_2$ NWs and SiO$_2$@Ag@OC–TiO$_2$ NWs were mixed at a specific weight ratio (total weight: 0.2 g) and dissolved in absolute ethanol (10 mL) and then sonicated for several hours to totally dispersed the NWs in the solvent. After sonication, ethyl cellulose (0.1 g, Sigma–Aldrich) dissolved in 10 mL of absolute ethanol was mixed with the solution of the OC–TiO$_2$ NWs. The mixture was stirred for 1 h and then sonicated overnight. Terpinol (0.869 mL, Sigma–Aldrich) was added to the solution. The mixture was evaporated to dryness using a rotary evaporator at 50 °C and 150 mPa.

Device fabrication

Patterned FTO glass (Pilkington, TEC–15, 15 Ω/sq) was fabricated as follows: FTO-coated glass was etched by 1 M of hydrochloric acid (HCl, 37 %, Sigma–Aldrich) with Zn powder (Sigma–Aldrich), and cleaned by sonication in a commercial detergent solution for 30 min followed by consecutively washing with deionized water, acetone and 2-propanol. A mildly acidic solution of titanium isopropoxide (97 %, Sigma–Aldrich) in absolute ethanol (a mixture of 14.5 mL of absolute ethanol with 1 mL of titanium isopropoxide and 0.15 mL of 37 % HCl solution) was spin-coated on the FTO substrate at 5,000 rpm for 10 s and annealed at 500 °C for 30 min on a hot plate to provide a 50-nm-thick compact blocking layer. The TiO$_2$-based ETL was then spin-coated on the blocking layer using the prepared paste diluted in absolute ethanol. The mass ratio of

the prepared paste and absolute ethanol was adjusted to control the thickness of the OC–TiO$_2$ NWs or TiO$_2$ NPs (18NR–T, Dyesol). After annealing a TiO$_2$-coated electrode at 500 °C for 30 min on a hot plate, it was post-treated for improving inter-connectivity with 0.02 M aqueous TiCl$_4$ (Sigma-Aldrich, > 98 %) at 70 °C for 20 min and annealed at 500 °C for 30 min. CH$_3$NH$_3$I was synthesized by the method reported elsewhere using methylamine (40 wt% in water, Sigma–Aldrich) and hydriodic acid (57 wt% in water, Sigma–Aldrich).[1] The perovskite precursor solution consisting of a 1:3 molar ratio of PbCl$_2$:CH$_3$NH$_3$I in DMF was prepared and pre-warmed at 60 °C. The mixture (40 wt%) was spin-coated on the post-treated mesoporous TiO$_2$ layer at 2,000 rpm for 40 s followed by annealing the wet film at 100 °C for 45 min to provide a dense perovskite film. After the deposition of the perovskite, 15 μL of spiro-MeOTAD (Lumtec) solution was spin-coated at 4,000 rpm for 30 s. The hole transport solution was prepared by dissolving 56 mg of spiro-MeOTAD in 1 mL of chlorobenzene, to which 12.3 μL of lithium bis(trifluoromethane)-sulfonimide (Li-TFSI) solution (520 mg in 1 mL of acetonitrile, Sigma–Aldrich) and 20.16 μL of 4-tert-butyl pyridine (Sigma–Aldrich) were added. Finally, a 60-nm-thick gold coating was deposited on the HTM layer by thermal evaporation. A typical active area of a cell was *ca.* 0.105 cm^2 as defined by a shadow mask.

Characterization

Current–voltage (J–V) curves of PSCs were measured using a 530 W xenon lamp (XIL Model 05A50KS source units; AM 1.5 solar irradiance; intensity: 100 mW/cm^2). The EQE was measured from 300–850 nm (PV Measurements, Boulder, CO, USA) under a short-circuit current. The morphology of the OC–TiO$_2$ NWs was revealed by TEM (JEOL JEM–200CX; JEOL Ltd., Tokyo, Japan). FE-SEM images were taken with a JEOL 6700 instrument. XRD patterns of the perovskite and TiO$_2$ were measured with an M18XHF–SRA instrument (Mac Science, Buffalo, NY, USA) using a Cu Kα radiation source (λ = 1.5406 Å) at 40 kV and 300 mA (12 W). UV–Vis absorbance spectra were collected by a Lambda–35 spectrometer (Perkin–Elmer, Waltham, MA, USA). Brunauer–Emmett–Teller (BET) surface areas and Barrett–Joyner–Halenda (BJH) pore size distributions of TiO$_2$ NP and OC-TiO$_2$ NW-based films were measured using a Micromeritic analyzer (ASAP 2000, Micromeritic Co., USA). Time-resolved photoluminescence was obatined by a compact fluorescence lifetime spectrometer (Quantaurus-Tau C11367-12, HAMAMATSU). The films were photo-excited by picosecond light pulser (PLP-10, HAMAMATSU). The laser wavelength was 464 nm with peak power of 231 mW and pulse duration of 53 ps. EIS measurements were recorded under a light illumination of 100 mW/cm^2 or in the dark using a Zahner Electrik IM6 analyzer (Zahner Electrik GmbH & Co., KG, Kronach, Germany).

Acknowledgements

Notes and references

1. H.-S. Kim, C.-R. Lee, J.-H. Im, K.-B. Lee, T. Moehl, A. Marchioro, S.-J. Moon, R. Humphry-Baker, J.-H. Yum, J. E. Moser, M. Grätzel and N.-G. Park, *Sci. Rep.*, 2012, **2**, 591.
2. J.-H. Im, C.-R. Lee, J.-W. Lee, S.-W. Park and N.-G. Park, *Nanoscale*, 2011, **3**, 4088-4093.
3. G. Niu, X. Guo and L. Wang, *J. Mater. Chem. A*, 2015, **3**, 8970-8980.
4. G. Giorgi and K. Yamashita, *J. Mater. Chem. A*, 2015, **3**, 8981-8991.
5. W. S. Yang, J. H. Noh, N. J. Jeon, Y. C. Kim, S. Ryu, J. Seo and S. I. Seok, *Science*, 2015, **348**, 1234-1237.
6. J. H. Heo, H. J. Han, M. Lee, M. Song, D. H. Kim and S. H. Im, *Energy Environ. Sci.*, 2015, **8**, 2922-2927.
7. T. Leijtens, B. Lauber, G. E. Eperon, S. D. Stranks and H. J. Snaith, *J. Phys. Chem. Lett.*, 2014, **5**, 1096-1102.
8. W. Zhang, M. Saliba, S. D. Stranks, Y. Sun, X. Shi, U. Wiesner and H. J. Snaith, *Nano Lett.*, 2013, **13**, 4505-4510.
9. J. Zhang, P. Barboux and T. Pauporté, *Adv. Energy Mater.,* 2014, **4,** 1400932.
10. Z. Zhu, X. Zheng, Y. Bai, T. Zhang, Z. Wang, S. Xiao and S. Yang, *Phys. Chem. Chem. Phys.,* 2015, **17**, 18265-18268.
11. K. Mahmood, B. S. Swain, A. R. Kirmani and A. Amassian, *J. Mater. Chem. A*, 2015, **3**, 9051-9057.
12. J.-F. Li, Z.-L. Zhang, H.-P. Gao, Y. Zhang and Y.-L. Mao, *J. Mater. Chem. A*, 2015, **3**, 19476-19482.
13. M. He, D. Zheng, M. Wang, C. Lin and Z. Lin, *J. Mater. Chem. A*, 2014, **2**, 5994-6003.
14. M. Yang, R. Guo, K. Kadel, Y. Liu, K. O'Shea, R. Bone, X. Wang, J. He and W. Li, *J. Mater. Chem. A*, 2014, **2**, 19616-19622.
15. S. Dharani, H. K. Mulmudi, N. Yantara, P. T. Thu Trang, N. G. Park, M. Graetzel, S. Mhaisalkar, N. Mathews and P. P. Boix, *Nanoscale*, 2014, **6**, 1675-1679.
16. H.-S. Kim, J.-W. Lee, N. Yantara, P. P. Boix, S. A. Kulkarni, S. Mhaisalkar, M. Grätzel and N.-G. Park, *Nano Lett.*, 2013, **13**, 2412-2417.
17. W. Q. Wu, F. Huang, D. Chen, Y. B. Cheng and R. A. Caruso, *Adv. Funct. Mater.,* 2015, **25**, 3264-3272.
18. D. Zhong, B. Cai, X. Wang, Z. Yang, Y. Xing, S. Miao, W. H. Zhang and C. Li, *Nano Energy*, 2015, **11**, 409-418.
19. Y. Yue, T. Umeyama, Y. Kohara, H. Kashio, M. Itoh, S. Ito, E. Sivaniah and H. Imahori, *J. Phys. Chem. C*, 2015, **119**, 22847-22854.
20. H.-L. Yip and A. K. Y. Jen, *Energy Environ. Sci.,* **5**, 5994-6011.
21. R. A. Naphade, M. Tathavadekar, J. P. Jog, S. Agarkar and S. Ogale, *J. Mater. Chem. A*, 2014, **2**, 975-984.
22. J. Yun, S. H. Hwang and J. Jang, *ACS Appl. Mater. Interfaces,* 2015, **7**, 2055-2063.
23. S. H. Hwang, D. H. Shin, J. Yun, C. Kim, M. Choi and J. Jang, *Chem. Eur. J.,* 2014, **20**, 4439-4446.
24. Z. Yuan, Z. Wu, S. Bai, Z. Xia, W. Xu, T. Song, H. Wu, L. Xu, J. Si, Y. Jin and B. Sun, *Adv.Energy Mater.*, 2015, **5,** 1500038.
25. H. A. Atwater and A. Polman, *Nat Mater*, 2010, **9**, 205-213.
26. S. H. Hwang, J. Roh, J. Lee, J. Ryu, J. Yun and J. Jang, *J. Mater. Chem. A*, 2014, **2**, 16429-16433.
27. C. Dong, W. Xiang, F. Huang, D. Fu, W. Huang, U. Bach, Y.-B. Cheng, X. Li and L. Spiccia, *Nanoscale*, 2014, **6**, 3704-3711.
28. K. Park, Q. Zhang, D. Myers and G. Cao, *ACS Appl. Mater. Interfaces*, 2013, **5**, 1044-1052.
29. Y. Zhao, A. M. Nardes and K. Zhu, *Faraday Discuss.*, 2014, **176**, 301-312.
30. S. D. Stranks, G. E. Eperon, G. Grancini, C. Menelaou, M. J. P. Alcocer, T. Leijtens, L. M. Herz, A. Petrozza and H. J. Snaith, *Science*, 2013, **342**, 341-344.
31. H. Choi, W. T. Chen and P. V. Kamat, *ACS Nano*, 2012, **6**, 4418-4427.
32. J. A. Schuller, E. S. Barnard, W. Cai, Y. C. Jun, J. S. White and M. L. Brongersma, *Nat Mater.*, 2010, **9**, 193-204.
33. S. Pillai, K. R. Catchpole, T. Trupke and M. A. Green, *J. Appl. Phys.*, 2007, **101**, 093105.
34. S.-J. Ko, H. Choi, W. Lee, T. Kim, B. R. Lee, J.-W. Jung, J.-R. Jeong, M. H. Song, J. C. Lee, H. Y. Woo and J. Y. Kim, *Energy Environ. Sci.*, 2013, **6**, 1949-1955.
35. W. L. Liu, F. C. Lin, Y. C. Yang, C. H. Huang, S. Gwo, M. H. Huang and J. S. Huang, *Nanoscale*, 2013, **5**, 7953-7962.
36. C. Su, L. Liu, M. Zhang, Y. Zhang and C. Shao, *CrystEngComm*, 2012, **14**, 3989-3999.
37. M. D. Brown, T. Suteewong, R. S. S. Kumar, V. D'Innocenzo, A. Petrozza, M. M. Lee, U. Wiesner and H. J. Snaith, *Nano Lett.*, 2011, **11**, 438-445.
38. X. Li, M. Ibrahim Dar, C. Yi, J. Luo, M. Tschumi, S. M. Zakeeruddin, M. K. Nazeeruddin, H. Han and M. Grätzel, *Nat Chem.*, 2015, **7**, 703-711.
39. Y. Yu, Y. Li, D. Geng, J. Wang, L. Zhang, T. L. Andrew, M. S. Arnold and X. Wang, *ACS Nano*, 2015, **9**, 564-572.
40. A. Marchioro, A. Dualeh, A. Punzi, M. Grätzel and J.-E. Moser, *J. Phys. Chem. C*, 2012, **116**, 26721-26727.
41. S. H. Hwang, J. Roh and J. Jang, *Chem. Eur. J.*, 2013, **19**, 13120-13126.
42. J. M. Marin-Beloqui, L. Lanzetta and E. Palomares, *Chem. Mater.*, 2016, **28**, 207-213.
43. G. Niu, W. Li, F. Meng, L. Wang, H. Dong and Y. Qiu, *J. Mater. Chem. A*, 2014, **2**, 705-710.
44. M. Hu, L. Liu, A. Mei, Y. Yang, T. Liu and H. Han, *J. Mater. Chem. A*, 2014, **2**, 17115-17121.
45. K. Guo, M. Li, X. Fang, X. Liu, B. Sebo, Y. Zhu, Z. Hu and X. Zhao, *J. Power Sources*, 2013, **230**, 155-160.
46. H. Zhou, Q. Chen, G. Li, S. Luo, T. B. Song, H. S. Duan, Z. Hong, J. You, Y. Liu and Y. Yang, *Science*, 2014, **345**, 542-546.
47. H. B. Wu, H. H. Hng and X. W. D. Lou, *Adv. Mater.*, 2012, **24**, 2567-2571.
48. S. H. Hwang, H. Song, J. Lee and J. Jang, *Chem. Eur. J.,* 2014, **20**, 12974-12981.

Graphical abstract
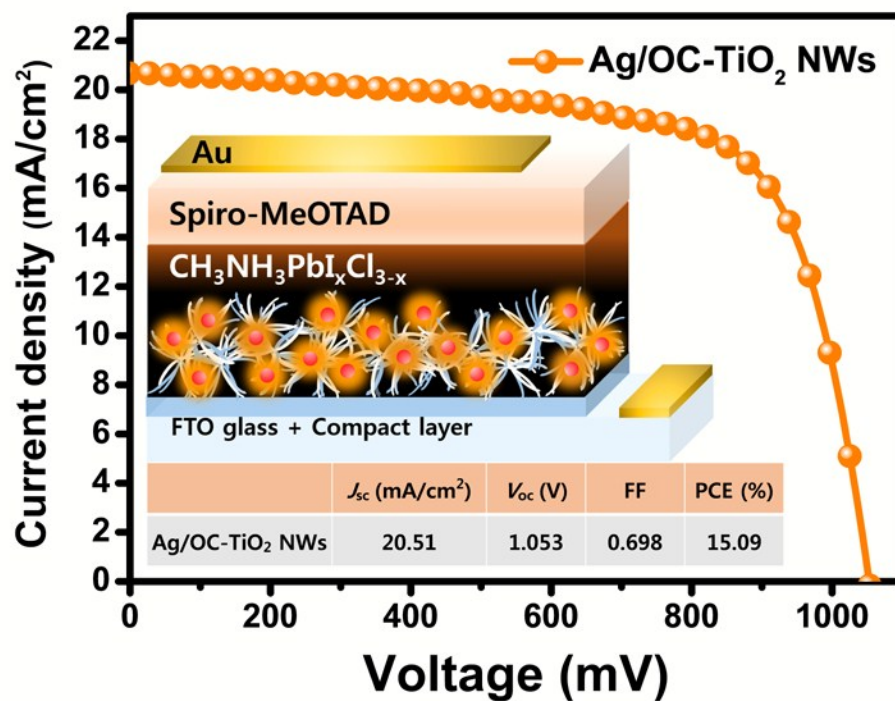
A perovskite solar cell based on collaborative scaffold structure consisting of orchid-like TiO_2 nanowires (OC-TiO_2 NWs) and silica-coated Ag@OC-TiO_2 NWs exhibited the best power conversion efficiency of 15.09 %.